

Improving the Physicochemical Properties of Fe–25Cr Ferritic Steel for SOFC Interconnects via Y-Implantation and Y_2O_3 -Deposition

Tomasz Brylewski · Aleksander Gil · Anna Rakowska ·
Sebastien Chevalier · Anna Adamczyk · Jarosław Dabek ·
Andrzej Kruk · Mirosław Stygar · Kazimierz Przybylski

Received: 11 August 2012 / Revised: 6 December 2012 / Published online: 30 December 2012
© The Author(s) 2012. This article is published with open access at Springerlink.com

Abstract The present study investigated the role of the reactive-element effect (REE) in improving the corrosion resistance, chromium vaporization rate, and electrical conductivity of the Fe–25Cr ferritic steel modified either by means of yttrium implantation or chemical deposition of yttrium oxide from metalloorganic compound vapors. The corrosion kinetics of the Fe–25Cr steel, both pure and modified, were determined under isothermal conditions in air and an Ar–H₂–H₂O gas mixture at 1,073 K. A significant improvement in corrosion resistance was observed after surface modification. XRD and SEM–EDS investigations showed that the protective Cr₂O₃ layer formed the main part of the scale. Measurements of Cr vaporization rate in the air–H₂O gas mixture revealed that both surface modifications of the steel significantly suppressed the formation of volatile chromium compounds to a large degree. The yttrium-implanted steels oxidized both in air and the Ar–H₂–H₂O mixture were characterized by the lowest area specific resistance and thereby did not exceed the acceptable ASR level ($0.1 \Omega \text{ cm}^2$) for interconnect materials in the temperature range of 973–1,073 K, unlike pure steel and the steel coated with Y₂O₃.

Keywords Solid oxide fuel cell (SOFC) · Metallic interconnect · Ferritic stainless steel · Reactive element effect · Kinetics · Chromia scale

T. Brylewski (✉) · A. Gil · A. Rakowska · A. Adamczyk · J. Dabek ·
A. Kruk · M. Stygar · K. Przybylski
Faculty of Materials Science and Ceramics, AGH University of Science and Technology,
Al. Mickiewicza 30, 30-059 Krakow, Poland
e-mail: brylew@agh.edu.pl

S. Chevalier
Institute Carnot Bourgogne ICB, CNRS UMR-5209-S.C., 9 Avenue Alain Savary, BP 47870,
21078 Dijon Cedex, France

Introduction

Planar-type solid oxide fuel cells (SOFCs) composed of ZrO_2 stabilized with Y_2O_3 (YSZ) are among the most promising designs for the motor industry on account of their high power output of up to 25 kW m^{-2} , simple geometry and compact size [1, 2]. Fuel cells connected in parallel feature interconnects in the form of bipolar plates, which serve the following functions: providing mechanical support within the cell, gas-tight separation of the cathode and anode spaces, ensuring electrical conduction between the cells, as well as the distribution of current to external devices. However, the design is hampered by one major flaw which cylindrical SOFCs are not affected. Namely, there are significant problems with ensuring sufficient tightness between the interconnect's plates and the remaining flat elements of the fuel cell. In effect, the durability of these devices is significantly decreased. Consequently, in the recent years many efforts have focused on developing technological solutions that would enable the production of planar-type SOFCs suitable for operation at low temperatures in the range of 873–1,073 K. In such a range of low temperatures fuel cell casings and interconnect plates may be composed of heat-resistant ferritic stainless steels (FSS), which are much cheaper than ceramic materials or expensive metallic alloys, whereas glass or silver may be used to ensure sufficient tightness [3]. Aside from offering advantages such as the ease of mechanical treatment, good weldability and high resistance to high-temperature corrosion in air (the atmosphere typical for the cathode space) and H_2 – H_2O , H_2 – H_2O – H_2S and CH_4 – H_2O gas mixtures (typical for the anode space), ferritic stainless steels also have a thermal expansion coefficient (TEC) similar to that of the anode material [4]. This makes it possible to construct anode supported cells (ASC).

During high-temperature oxidation of ferritic steel with a chromium content of up to 25 wt%, a two-layer scale is formed. The thin outer layer is composed of the MnCr_2O_4 spinel, while Cr_2O_3 forms the thick inner layer [5–10]. The spinel layer inhibits the formation of volatile chromium oxides and oxyhydroxides (mostly $\text{CrO}_2(\text{OH})_2$), which increase the activation polarization of the cathode [11]. The main issue faced when applying these steels in interconnect construction is the gradual increase in area specific resistance (ASR) connected with the growing thickness of the scale [5–10, 12]. An overly high resistance of the scale may significantly inhibit the flow of electric current from the cathode to the interconnect, which results in the decrease in the fuel cell's power output [2]. The growth rate of the Cr_2O_3 is therefore an important factor affecting the resistance of the SOFC, which should ideally be maintained at the lowest possible level throughout the cell's operation life. One of the ways in which this may be achieved is by triggering the so-called reactive element effect (REE).

Extensive experimental studies have shown that the addition of small amounts of active elements such as Y, La, Ce, Hf, Nd or their oxides, in the form of dispersed particles, is an effective method of improving the corrosion resistance of the alloys that form the protective Al_2O_3 or Cr_2O_3 scales. [13–15] Active elements improve the adhesion of the above-mentioned scales to the metallic phase, and in the case of the Cr_2O_3 scale additionally decrease its growth rate. It is therefore to be expected

that as the thickness of the compact chromia scale decreases, so will the electrical resistance of the steel/scale system, since its electrical properties are determined predominantly by the physicochemical properties of chromia itself, as well as the surface area of its contact with the metallic core [16].

The aim of the present paper was to determine the combined effect of the REE and the heat-treatment atmosphere on the corrosion resistance, chromium vaporization rate and electrical conductivity of the Fe–25Cr steel modified by means of yttrium implantation or deposition of yttria on its surface using metalloorganic chemical vapor deposition (MOCVD).

Experimental Procedures

Preparation of Samples

The ferritic steel Fe–25Cr 17153.2 CSN EN 10204 3.1.B (DIN 50049) (Valcovny Plechu a.s. Frydek-Mistek, Czech Republic) with the composition of Cr-24.55, Mn-0.28, Si-0.74, Ni-0.99, C-0.04, P-0.03, S-0.013 and Ti-0.01 wt% was used in the investigations. Experiments on oxidation featured two kinds of samples of the above-mentioned material: (1) rectangular samples with the approximate dimensions of $20 \times 10 \times 0.5$ mm cut from metal sheets were used to study the oxidation kinetics of pure steel and steel either implanted with yttrium or with a deposited Y_2O_3 layer; (2) square samples with a total surface area of 2 cm^2 and a thickness of ca. 0.1 cm were used in the measurements of electrical resistance and the rate of chromium volatilization. The chromium volatilization rate was also measured for the Fe–25Cr model alloy, which was treated as a reference material for steel. The surfaces of the samples were ground with 100–1,200 grade SiC abrasive paper, and then polished in an aqueous Al_2O_3 slurry with a mean gradation of $0.3 \mu\text{m}$ until a mirror-like was obtained. The samples were then rinsed using water with a detergent and ethyl alcohol, and degreased in acetone by means of an ultrasonic washer.

Yttrium was implanted underneath the surface of the Fe–25Cr steel by means of ion beam implantation (IBI) using the apparatus owned by the Polish Academy of Sciences' Institute of Nuclear Physics in Krakow [17]. Depending on the intended application, the samples were implanted either on one side only (for morphological observations) or on both sides (for kinetics and electrical resistance studies). Plasma containing ionized yttrium was obtained via glow discharge in YCl_3 vapors. A beam of singly ionized yttrium atoms—Y—was accelerated to the energy level of 25 keV using 1×10^{16} Y ions per cm^2 . The distribution of the implanted yttrium ions calculated based on the Lindhard-Scharf-Schiott (LSS) model was Gaussian-like. The highest concentration of yttrium for the above-specified ion dose was equal to 12.7 at.%, while the effective range of yttrium ions was 17.3 nm.

During the deposition of the Y_2O_3 oxide on the surface of the Fe–25Cr steel performed by means of metalloorganic chemical vapor deposition, $T((\text{tmRd})_3\text{Y})$ was used as the metalloorganic precursor [18]. This precursor and N_2 carrier gas at 483 K were introduced into the reactor's chamber at a flow rate of $125 \text{ cm}^3 \text{ min}^{-1}$, along with oxygen supplied at a rate of $42 \text{ cm}^3 \text{ min}^{-1}$. In the reactor yttrium was

deposited directly on the steel substrate, which was heated up to 873 K for 25 min. A thin layer with 180 nm average thickness of yttria formed as a result of the reaction between yttrium and oxygen. In order to distribute yttrium evenly across the steel surface, the substrate was rotated around its axis. Surface modification by means of the MOCVD method was carried out at the Institute Carnot de Bourgogne (ICB) in Dijon, France.

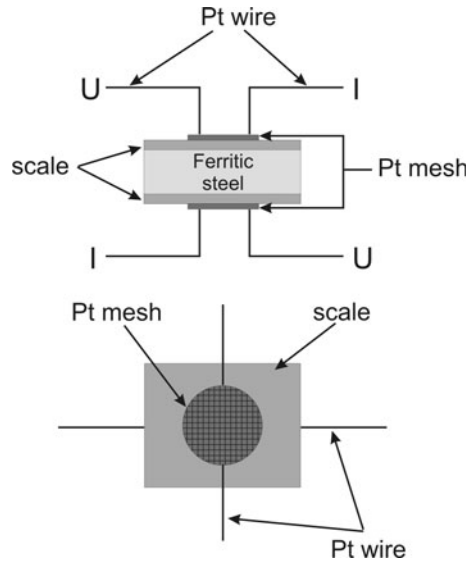
Oxidizing Procedure and Methods of Sample Characterization

Oxidation studies of the Fe–25Cr steel, pure and modified using Y and Y_2O_3 were carried out in isothermal conditions. The investigated atmospheres were laboratory air and the Ar– H_2 – H_2O gas mixture with a $p(H_2)/p(H_2O)$ ratio equal to 94/6, at a temperature of 1,073 K and for oxidation times of up to 300 h. Isothermal oxidation of samples was investigated using the thermogravimetric method, which made it possible to continuously monitor their mass gain by means of the MK2 Vacuum Head Microbalance supplied by CI Electronics (UK) with an accuracy of the order of 10^{-6} g. The setup used for the measurement of oxidation kinetics together with the flow system needed to obtain the Ar– H_2 – H_2O gas mixture is described in detail in [19].

The rate of chromium vaporization from the ferritic steel, pure and surface-modified, was measured using the transpiration method and flow conditions for the air– H_2O mixture containing 10 % water vapor by volume. The measurements were carried out for 100 h at 1,073 K. The Fe–25Cr alloy was used as a reference material. The applied methodology is described in [20].

Electrical resistance measurements of the studied samples were conducted by means of a *dc* 2-probe 4-point method using an outer current source; this parameter was expressed as a function of temperature in the range from 573 to 1,073 K, using a current intensity of 0.01 A and laboratory air. The resistance was determined on the basis of Ohm's law. Figure 1 shows a schematic diagram of the setup used for the measurement of the samples' resistance. Before the measurements, two specimens representing each of the three types of the studied samples were pre-oxidized at 1,073 K for 300 h in two different atmospheres: air or the Ar– H_2 – H_2O gas mixture, yielding six different samples. Both sides of the oxidized samples were covered with platinum paste (Heraeus), followed by placing platinum meshes with a surface area of 19 mm^2 on top of the pastes. The mesh played the role of a current collector. The sample prepared in this 'sandwich' system was placed between two-plane Pt electrodes and the voltage drop was measured using a current supplier (JOTA). The current drop for each sample was measured using an HP digital multimeter (34,401 A) with 0.3 % precision. Each measurement of the electrical resistance was conducted and verified for reproducibility at a constant temperature over a short time to avoid further oxidation of the samples in air. To avoid the expected scale growth related to the oxidation of the steel in the course of electrical resistance measurements, an attempt was made to reduce the duration of the measurements by as much time as possible, as suggested elsewhere [21]. Sample resistance was therefore recorded at the given temperature every 10 min. The

Fig. 1 Schematic diagram of the ASR measurement setup utilizing the *dc* 2-probe 4-point method



temperature was then increased by 25 K and the sample was equilibrated at this increased temperature for 1 h.

The electrical resistance of an oxidized specimen is usually measured in terms of its ASR, since the exact thickness of an oxide formed on a metallic surface is difficult to determine. Therefore, the ASR of the samples was calculated based on the obtained resistance values using the following formula:

$$\text{ASR} = \frac{R \cdot A}{2} \quad (1)$$

where R is the electrical resistance [Ω], and A is the surface area of the Pt layer [cm^2].

The phase composition of the products of oxidation of the pure and surface-modified steel was studied by means of X-ray diffraction (XRD) performed with the X'Pert XRD diffractometer (Panalytical), carried out using $\text{CuK}\alpha$ radiation at a scan rate of 0.008° per step. The morphology and chemical composition of the samples were investigated by means of scanning electron microscopy (SEM) performed using a FEI Nova Nano SEM 200 microscope coupled with an EDAX system required for chemical composition analysis via energy-dispersive X-ray spectroscopy (EDS). Conventional transmission electron microscopy (TEM) and selected-area diffraction (SAD) using Philips CM 20 at 200 kV were also applied to study the microstructure of the samples. Due to the thickness of the scales, which was at times as low as a fraction of micrometer, the transverse fractures of the samples used in this study were obtained in liquid nitrogen.

Results and Discussion

Oxidation Kinetics of Pure Versus Surface-Modified Fe–25Cr Steel

The research conducted thus far indicates that over a relatively wide range of temperatures the oxidation rate of ferritic steels containing chromium and other alloy additions is inversely proportional to the thickness of the Cr_2O_3 scale and may be expressed by a dependence called the parabolic rate law [22]

$$\frac{dx}{dt} = \frac{k_p}{x} \quad (2)$$

where k_p is the parabolic rate constant of the oxidation [$\mu\text{m}^2 \text{s}^{-1}$], x is the thickness of scale layer [μm] over time t [s].

By integrating Eq. (2) a graphic form more suitable for interpretation may be obtained

$$x^2 = 2k_p t + C_{(x)} \quad (3)$$

where $C_{(x)}$ is the integration constant, a measure of deviation from parabolic oxidation kinetics in the initial stage.

The growth of Cr_2O_3 scales are usually measured by determining the mass of oxygen bound per unit of metal surface area. Since the thickness of the product layer is directly proportional to the above-mentioned mass of the oxidant, for the purpose of drawing kinetic plots and using them to calculate parabolic oxidation rate constants Eq. (3) may be transformed into the form given by Pilling and Bedworth and quoted by Mrowec and Werber [23]

$$\left(\frac{\Delta m}{A}\right)^2 = k_g t + C_{(y)} \quad (4)$$

where Δm is the mass gain of the oxidized sample [g], A is the surface area of the sample [cm^2], k_g is the parabolic oxidation rate constant [$\text{g}^2 \text{cm}^{-4} \text{s}^{-1}$].

When ferritic steel is oxidized in different oxidation conditions a two-phase scale is formed (as opposed to a compact single-phase one), with two separate layers: a thin outer layer composed of $(\text{Mn,Cr})_3\text{O}_4$ and a thick inner layer composed of Cr_2O_3 . If it is assumed that the growth of such a reaction product on a metallic substrate approximately obeys the parabolic rate law, then k_p in Eq. (3) should be replaced with the 'effective parabolic rate constant', $k_{p,ef}$ [24]. Since the scale formed on such steel is composed mostly of Cr_2O_3 , its approximate thickness may be estimated using the dependence

$$x_z^2 = 2k_{p,ef} t \quad (5)$$

based on the relation between the thickness of the Cr_2O_3 scale and the mass change of the sample, determined during thermogravimetric measurements as [22]

$$\Delta m = x_z A \rho_{\text{Cr}_2\text{O}_3} \frac{3/2 M_{\text{O}_2}}{M_{\text{Cr}_2\text{O}_3}} \quad (6)$$

where $\rho_{\text{Cr}_2\text{O}_3}$ is the density of chromia [g cm^{-3}], $M_{\text{Cr}_2\text{O}_3}$ is the molecular weight of the scale with Cr_2O_3 [g mol^{-1}], M_{O_2} is the molecular weight of oxygen [g mol^{-1}].

The oxidation of ferritic steels is often a complex process, since its rate is determined not only by external factors, but also by the structure and phase and chemical compositions of the reaction products formed at the steel-oxidant phase boundary. During oxidation of such steels the mechanism of scale formation may change; in such a case the same metal may oxidize with different kinetics [23]. These deviations from the fixed oxidation kinetics may be illustrated using the instantaneous values of parabolic oxidation rate constants (k_g^i). If the character and physicochemical properties of the scale remain constant during kinetic investigations then the parabolic oxidation rate constant k_g^i assumed for a particular process is independent of oxidation time. By adding the instantaneous values of parabolic rate constants (k_g^i) in the range of measurements, according to the dependence [25]

$$k'_g = \sum_{i=1}^{N-1} \left(\frac{k_g^i + k_g^{i+1}}{2} \right) \left(\frac{t_{i+1} - t_i}{t_N - t_{i+1}} \right) \quad (7)$$

where k_g^i is the instantaneous parabolic rate constant [$\text{g}^2 \text{cm}^{-4} \text{s}^{-1}$] and N is the number of measuring points, the resultant value of the parabolic rate constant, k'_g , may be determined (expressed in [$\text{g}^2 \text{cm}^{-4} \text{s}^{-1}$]). If scale growth obeys the parabolic rate law over the investigated range of temperatures and partial pressures, then the ratio of k'_g to k_g is equal to 1 or close to this value.

Figure 2 shows the oxidation kinetics of the Fe–25Cr steel, pure and surface-modified through yttrium implantation (Fe–25Cr/Y) or the deposition of yttria using MOCVD (Fe–25Cr/Y₂O₃) expressed as mass change (Fig. 2a) and squared mass change (Fig. 2b) in a function of time; the curves also express scale thickness as a function of reaction time. Corrosion of these samples was carried out in air and the Ar–H₂–H₂O gas mixture at 1,073 K for 300 h. Table 1, in turn, shows their corresponding parabolic oxidation rate constants obtained using the graphic method. The presented kinetic plots (Fig. 2) do not include the correction for the formation of volatile chromium compounds. When this effect is not taken into account the relative error for times that do not exceed 1,200 h is lower than 3 %. Scale thickness values calculated from dependence (5) based on mass gain are consistent with the mean scale thickness values estimated from metallographic polished sections. For the calculations it was assumed that the density of chromia is equal to 5.225 g cm⁻³ and, furthermore, that Cr₂O₃ is the predominant component of the scale (Subsect. 3.3).

The plots presented in Fig. 2 and the values of the k'_g/k_g ratio (Table 1) suggest that, with the exception of the incubation period, the oxidation kinetics of the Fe–25Cr, Fe–25Cr/Y and Fe–25Cr/Y₂O₃ steels under different conditions approximately obey the parabolic rate law. Fe–25Cr steels with 1×10^{16} yttrium ions implanted per cm² and those coated with a Y₂O₃ layer are characterized by significantly higher corrosion resistance than pure steel (Fig. 2), regardless of the type of atmosphere the reaction takes place in. The data collected in Table 1 indicates that the parabolic oxidation rate constant of the Fe–25Cr/Y steel is approximately half an order of magnitude lower than the corrosion rate constant of

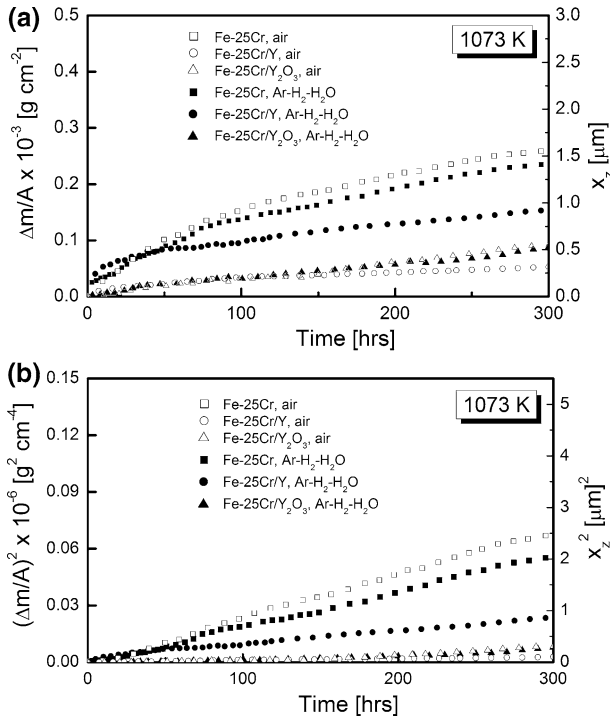


Fig. 2 Oxidation kinetics of Fe–25Cr, Fe–25Cr/Y and Fe–25Cr/Y₂O₃ steel samples in air and Ar–H₂–H₂O at 1,073 K expressed as mass change (a) and squared mass change (b) in a function of time

Fe–25Cr/Y₂O₃ when oxidation occurs in air; however, for reduced oxygen pressure, i.e. in the Ar–H₂–H₂O mixture, the opposite is true. As far as the pure Fe–25Cr steel is concerned, the oxidation rate of Fe–25Cr/Y is less than one order of magnitude lower after oxidation in air and half an order of magnitude lower after oxidation in the Ar–H₂–H₂O gas mixture.

The research conducted thus far by other authors [14, 26–29] confirm that surface modification of the investigated steel via Y ion implantation or Y₂O₃ deposition by means of MOCVD significantly affects the kinetics of their isothermal oxidation.

Investigations of the Rate of Chromium Volatilization from the Surface of the Products of Oxidation of Pure and Surface-Modified Fe–25Cr Steel

In order to evaluate the effectiveness of surface modification of the Fe–25Cr steel in terms of its ability to suppress the emission of volatile chromium compounds (such as CrO₂(OH)₂) from its surface during oxidation in conditions of the SOFC cathode working space, studies on the volatilization rate of chromium were carried out. These investigations were performed using the transpiration method at a temperature of 1,073 K, a time of 100 h, in flow conditions with the flow rate of air equal 120 cm³ min^{−1}, and air containing water vapor with a partial pressure, $p(\text{H}_2\text{O})$,

Table 1 Parabolic oxidation rate constants for Fe–25Cr, Fe–25Cr/Y and Fe–25Cr/Y₂O₃ steels at 1,073 K in different oxidizing atmospheres

Material	Oxidizing atmosphere	Time [h]	k_g [g ² cm ⁻⁴ s ⁻¹]	$k_{p,ef}$ [μm ² s ⁻¹]	k'_g [g ² cm ⁻⁴ s ⁻¹]	k'_g/k_g
Fe–25Cr	Air	50–300	6.48×10^{-14}	1.20×10^{-6}	6.59×10^{-14}	1.02
Fe–25Cr	Ar–H ₂ –H ₂ O	15–300	5.39×10^{-14}	9.90×10^{-7}	5.20×10^{-14}	0.97
Fe–25Cr/Y	Air	5–300	2.44×10^{-15}	4.48×10^{-8}	2.37×10^{-15}	0.97
Fe–25Cr/Y	Ar–H ₂ –H ₂ O	10–300	1.92×10^{-14}	3.53×10^{-7}	2.08×10^{-14}	1.08
Fe–25Cr/Y ₂ O ₃	Air	8–300	7.09×10^{-15}	1.30×10^{-7}	6.95×10^{-15}	0.98
Fe–25Cr/Y ₂ O ₃	Ar–H ₂ –H ₂ O	5–300	6.82×10^{-15}	1.25×10^{-7}	7.02×10^{-15}	1.03

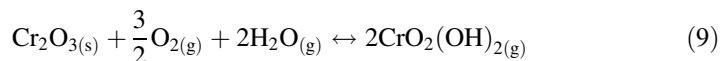
equal to 9.72×10^{-2} atm. The investigated materials were the reference alloy Fe–25Cr and the Fe–25Cr, Fe–25Cr/Y i Fe–25Cr/Y₂O₃ steels pre-oxidized for 100 h in air at 1,073 K.

Figure 3 presents a comparison of the measured rates of chromium volatilization from the surface of samples of the reference Fe–25Cr alloy and the Fe–25Cr steel, pure and surface-modified via Y implantation or Y₂O₃ deposition. The highest rate of chromium volatilization equal to 1.02×10^{-6} g m⁻² s⁻¹ was observed in the case of the Fe–25Cr alloy. After oxidation a scale composed entirely of chromia forms on the surface of this alloy [20]. Compared to the mass loss of the reference alloy, the mass loss recorded in the case of the Fe–25Cr ferritic steel investigated in the present paper was over 50 % lower. The reason behind the reduced rate of chromium volatilization from the surface of this steel is the presence of the Mn_{1.5}Cr_{1.5}O₄ spinel layer in the outer part of the scale composed of chromia.

Studies by Konyshева et al. [30, 31]. showed that the continuous (Mn,Cr)₃O₄ spinel layer formed in the outer part of the Cr₂O₃ scale during oxidation of the Crofer 22APU steel at 1,073 K reduces the chromium volatilization rate to less than one-third of that characteristic of the ODS alloy; in identical conditions the surface of this alloy is covered with a single-phase Cr₂O₃ scale. Since the activity of this oxide in MnCr₂O₄ drops to a level below 1, then according to the following equation [30]

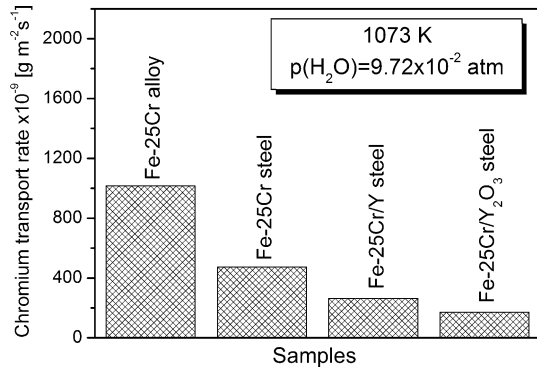
$$\ln p_{CrO_2(OH)_2} = -\frac{\Delta_{r(9)}H^\circ}{2R} \left(\frac{1}{T}\right) + C' + \ln a_{Cr_2O_3} \tag{8}$$

where $a_{Cr_2O_3}$ is the activity of the chromia, $\Delta_{r(9)}H^\circ$ is the standard change in the enthalpy of the reaction [J mol⁻¹] [11]



the partial pressure of volatile CrO₂(OH)₂ is also reduced. The formation of the spinel on the tested steel therefore leads to the expected decrease in the rate of Cr volatilization (Fig. 3).

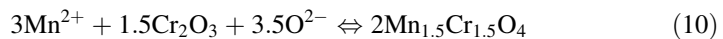
Fig. 3 Evaporation rate of chromia species on Fe–25Cr alloy and Fe–25Cr, Fe–25Cr/Y and Fe–25Cr/Y₂O₃ steels in humidified air at 1,073 K



As demonstrated by Fig. 3, the implantation of yttrium underneath the surface of the investigated ferritic steel or the deposition of yttria on it leads to a reduction (compared to steel with no surface modification) in chromium volatilization rate. The lowest chromium volatilization rate (over 50 % lower than the rate of mass loss of pure Fe–25Cr steel) was observed when the Y₂O₃ layer was deposited on the steel substrate by means of MOCVD. Consequently, it seems justified to carry out surface modification of the Fe–25Cr steel via ion implantation with active elements or to deposit protective layers that may effectively suppress the emission of volatile Cr particles in the working space of SOFC, especially on the cathode side. This problem is of fundamental important to the effective operation of SOFCs.

Microstructure and Chemical Composition of Oxidation Products Formed on Pure Fe–25Cr Steel and Surface-Modified Steel

Figure 4 shows the X-ray diffraction patterns of the Fe–25Cr, Fe–25Cr/Y and Fe–25Cr/Y₂O₃ steels oxidized in air at 1,073 K for 300 h (Fig. 4a) and the Ar–H₂–H₂O gas mixture (Fig. 4b). All X-ray diffraction patterns for the analyzed samples with the exception of the Fe–25Cr steel oxidized in air exhibit strong reflections of α -Fe originating from the substrate material, indicating the formation of very thin oxidation products. The scales formed on the surface of pure Fe–25Cr steel oxidized in different atmospheres consist of the Fe-doped Cr₂O₃ and Mn_{1.5}Cr_{1.5}O₄ spinel phases. The presence of iron in the chromia, confirmed by means of EDS analysis, is the result of the mutual solubility of Cr₂O₃ and Fe₂O₃ phases at 1,073 K, which is related to their analogous hexagonal structure and similar lattice parameters [32]. Furthermore, the formation of chromium manganese spinel is caused by the fast diffusion of manganese along the ferrite and chromia grain boundaries; on the surface, manganese reacts with the chromia that had initially been formed and the inwardly diffused oxygen anions to form the spinel phase, according to the following equation



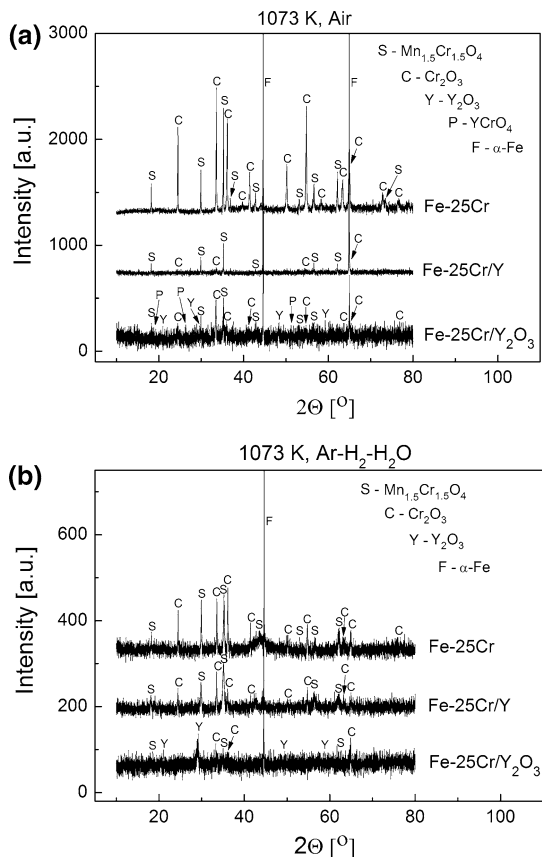
The above reaction is consistent with the report by Cox et al. [33], who showed that the diffusivities of metal ions in Cr₂O₃ decrease in the order

$D_{Mn} > D_{Fe} > D_{Ni} > D_{Cr}$, assuming that metals diffuse as ions via Cr^{3+} —lattice sites in Cr_2O_3 . Due to the fast diffusion of Mn ions in oxide scales from the steel to the scale surface, the $Mn_{1.5}Cr_{1.5}O_4$ spinel is formed as the outer layer of the scale. Only the Cr_2O_3 and $Mn_{1.5}Cr_{1.5}O_4$ phases were observed on the Fe–25Cr/Y steel oxidized in air and the Ar–H₂–H₂O mixture (Fig. 4a, b). The comparison of the XRD diffraction patterns for pure Fe–25Cr steel and the same steel implanted with Y revealed the presence of additional small reflexes, which can be attributed to the Y_2O_3 and $YCrO_4$ content in the scales formed on the Fe–25Cr/ Y_2O_3 steel exposed to air (Fig. 4a); on the other hand, only peaks of Y_2O_3 , Cr_2O_3 and $Mn_{1.5}Cr_{1.5}O_4$ were observed in the case of the Fe–25Cr/ Y_2O_3 sample oxidized in the Ar–H₂–H₂O mixture (Fig. 4b). It should be noted that the other $YCrO_4$ reflexes overlap with the reflexes of chromium oxide, so full identification is not possible. According to the valuable discussion shown in [29], the formation of $YCrO_4$ may be expressed as



The presence of Y_2O_3 and $YCrO_4$ phases had been confirmed by other authors applying Y-containing coatings on different ferritic steel [29, 34–36]. The formation

Fig. 4 X-ray diffraction patterns for the Fe–25Cr, Fe–25Cr/Y and Fe–25Cr/ Y_2O_3 samples obtained after 300 h of oxidation at 1,073 K in: **a** air and **b** Ar–H₂–H₂O



of these oxides may block grain boundary diffusion paths and thus significantly reduce the oxidation rate [29].

Figure 5 shows the surface morphology of the scales formed on pure Fe–25Cr, Fe–25Cr/Y and Fe–25Cr/Y₂O₃ steels after 300 h of oxidation in air at 1,073 K. SEM–EDS analyses revealed that the Mn_{1.5}Cr_{1.5}O₄ spinel phase had formed over the Fe-doped chromia scale, which was the main oxidation product. However, it is possible that the Fe signal originated from the steel substrate; the EDS analysis is carried out at the rather thin surface of the scale. Based on the EDS results, the ratio of Mn:Cr in the spinel phase is assumed to be 1.5:1.5. The scale formed on the pure Fe–25Cr steel oxidized in air is irregular and consists of the spinel in the form of thin continuous outer layers and separate and linear precipitates at grain boundaries of the steel; these precipitates feature a large number of Mn_{1.5}Cr_{1.5}O₄ crystallites with sizes ranging from 2 to 5 μm (Fig. 5a). The observation of the scale formed on the Fe–25Cr/Y steel after oxidation in air revealed a fine-grained morphology of the chromia layer. The surface of this sample contains a number of Mn_{1.5}Cr_{1.5}O₄ precipitates with sizes from 1 to 4 μm (Fig. 5b). In addition to isolated precipitates of the Mn_{1.5}Cr_{1.5}O₄ spinel, the products of oxidation of the Fe–25Cr/Y₂O₃ steel in air included a fine-crystalline protective layer consisting of Cr₂O₃ and Y₂O₃ (Fig. 5c), because the solubility of Y₂O₃ in Cr₂O₃ is negligible [14]. The presence of these phases was confirmed through X-ray analysis (Fig. 4a) and EDS point analyses, illustrated in Fig. 6. As can be seen, the underlying layer was composed of small crystallites of yttria and chromia (region 2-Fig. 6c) with a size of around 0.3 μm, while the size of the spinel precipitates (region 1-Fig. 6b) ranged from 1 to 12 μm.

Figure 7 presents the surface morphologies of the scales formed on pure Fe–25Cr and the Fe–25Cr/Y and Fe–25Cr/Y₂O₃ steels after oxidation in the Ar–H₂–H₂O gas mixture at 1,073 K for 300 h. The scales formed on the pure Fe–25Cr steel in the Ar–H₂–H₂O gas mixture were composed of chromia and the Mn_{1.5}Cr_{1.5}O₄ spinel and exhibited a coarse-crystalline morphology (Fig. 7a). The surface of the scale features a discontinuous outer spinel layer composed of oval agglomerates; between these agglomerates well-developed grains of chromium oxide in the form of thin plates created in the initial stages of oxidation of the studied steel may be discerned. The scale formed on the Fe–25Cr yttrium-implanted steel after oxidation in the gas mixture containing hydrogen and water, on the other hand, consisted of well-developed Cr₂O₃ particles in the form of thin plates and whiskers distributed in random directions (Fig. 7b). Based on the SEM microphotograph of the Fe–25Cr/Y steel oxidized in the Ar–H₂–H₂O mixture, shown in Fig. 8, the size and thickness of these plates were estimated at 2 and 0.1 μm, respectively. In this scale, the Mn_{1.5}Cr_{1.5}O₄ crystallites in the form of aggregates that cause the formation of “islands” were also identified. The fine-crystalline matrix of the scale formed on the Fe–25Cr/Y₂O₃ steel after its oxidation in the Ar–H₂–H₂O mixture was uneven and consisted of yttria and a small amount of chromia (Fig. 7c). In addition, separate precipitates of the Mn_{1.5}Cr_{1.5}O₄ spinel, with size ranging from 0.5 to 1.5 μm, were found (Fig. 7c).

Figure 9 shows the SEM microstructure of the fracture cross-section of scale formed on the Fe–25Cr steel after oxidation in air at 1,073 K for 300 h and a series

Fig. 5 SEM microphotographs of the surface of the scales formed on: **a** Fe–25Cr, **b** Fe–25Cr/Y and **c** Fe–25Cr/Y₂O₃ steels oxidized in air at 1,073 K for 300 h

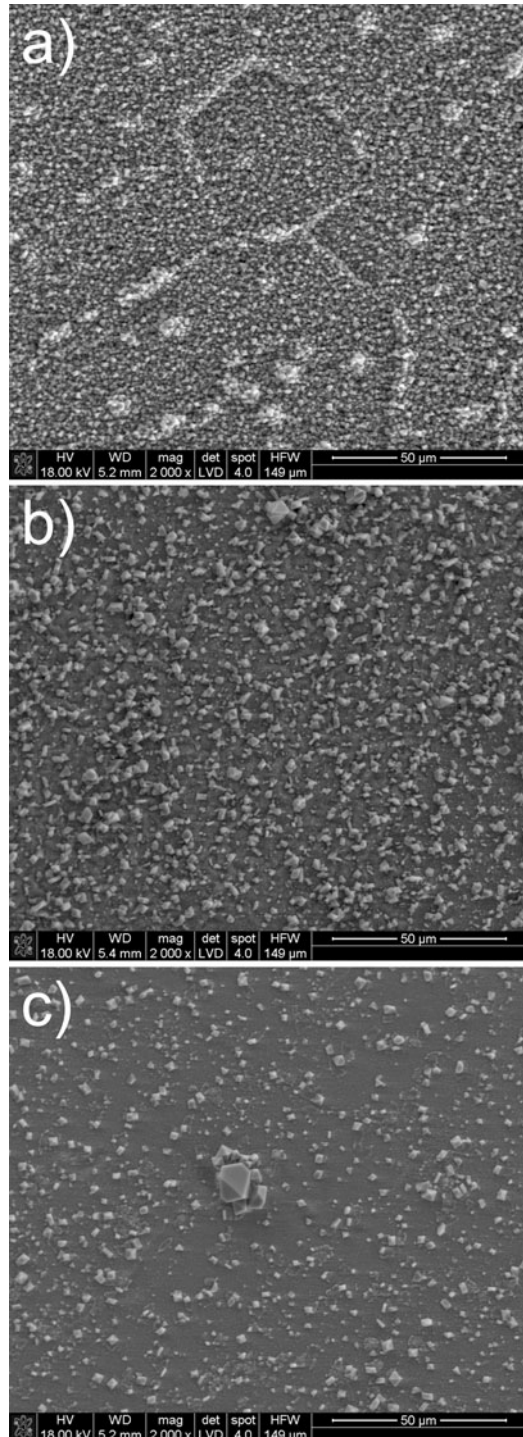


Fig. 6 **a** SEM microphotograph of the surface of the scale on Fe–25Cr/Y₂O₃ oxidized in air at 1,073 K for 300 h, **b, c** EDS point analyses of regions designated as *1* and *2*

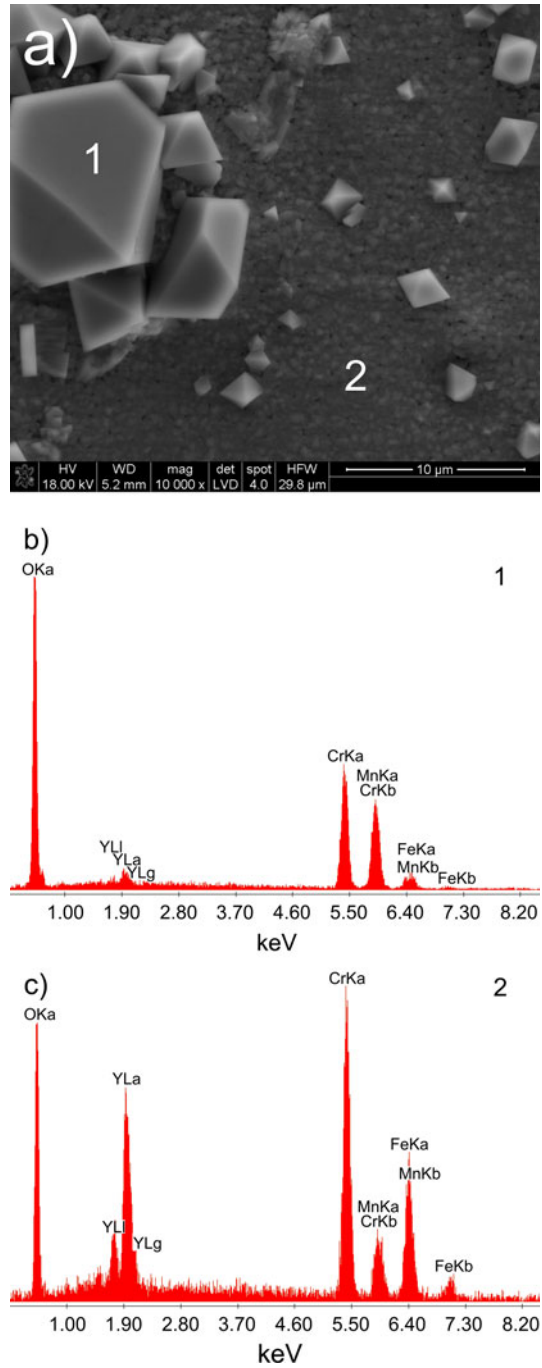


Fig. 7 SEM microphotographs of the surface of the scales formed on: **a** Fe–25Cr, **b** Fe–25Cr/Y and **c** Fe–25Cr/Y₂O₃ steels oxidized in Ar–H₂–H₂O at 1,073 K for 300 h

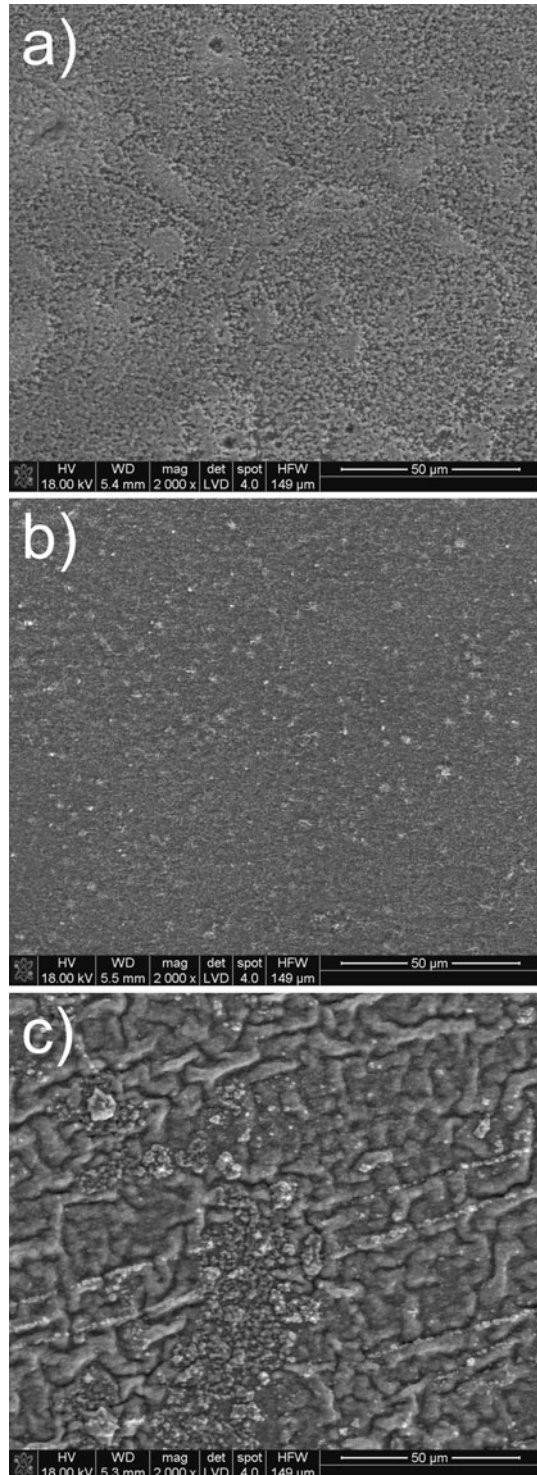
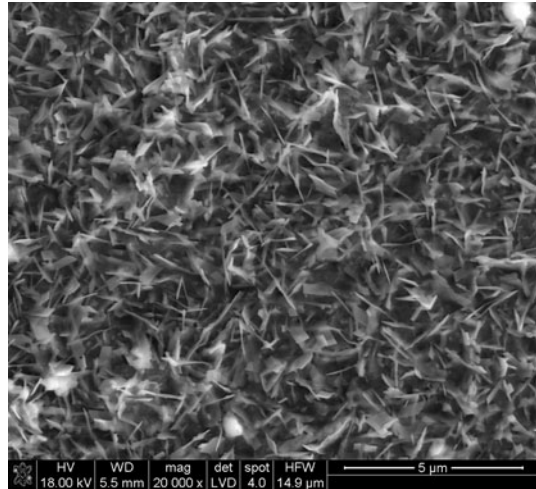


Fig. 8 SEM microphotograph of the surface of the scale formed on Fe–25Cr/Y oxidized in Ar–H₂–H₂O at 1,073 K for 300 h



of EDS point analyses. The resulting scale is two-layer and consists of a thick and continuous fine-crystalline inner layer built of chromia doped with Fe (Fig. 9c) and a thinner outer layer of Mn_{1.5}Cr_{1.5}O₄ (Fig. 9b). The average thickness of the (Cr,Fe)₂O₃ layer is about 1.5 μm, while that of the spinel layer is equal to about 0.2 μm. Scale thickness calculated from weight gain (Eq. (5)) is in good agreement with the average thickness of the scale estimated from the SEM morphology (Fig. 9a). It should be noted that the afore-mentioned main layer is compact and characterized by poor adhesion to the metallic core; in addition, the adhesion of the thin spinel layer to chromia is also unsatisfactory. On the one hand, this may be attributed to the effects of the Cr₂O₃ and Mn_{1.5}Cr_{1.5}O₄ dilatation, which are the result of different thermal expansion coefficients of these oxides, and on the other hand to the depletion of the reservoir of manganese in steel (this phenomenon is known as the depletion of minor alloying elements). EDS point analysis in the central part of the scale revealed significant concentrations of Cr and O with very little Fe content, which indicates the formation of a protective chromia scale of chromium oxide as a result of selective oxidation of chromium (Fig. 9c). A slight decrease in the concentration of Cr in the outer layer with a simultaneous increase in Mn content may entail the presence of the Mn_{1.5}Cr_{1.5}O₄ spinel layer (Fig. 9b).

It is worth to note that parts of the scales formed on pure Fe–25Cr steel after oxidation in air at 1,073 K bulge, which may be explained by a convolution effect [13] due to the appearance of mechanical stresses within the scale (Fig. 10). This phenomenon, known as a counter-current diffusion, takes place during the simultaneous inward diffusion of oxygen and predominant outward diffusion of chromium at the grain boundaries of the scale. When outward diffusion of interstitial chromium cations accounts for a major part of total mass transport throughout a growing scale, voids and cracks form near the steel/scale interface, which is associated with the Kirkendall–Frenkel effect [37]. In the absence of adequate scale adhesion to the metal core, spallation may occur during the oxidation of the Fe–25Cr steel with cyclic temperature change.

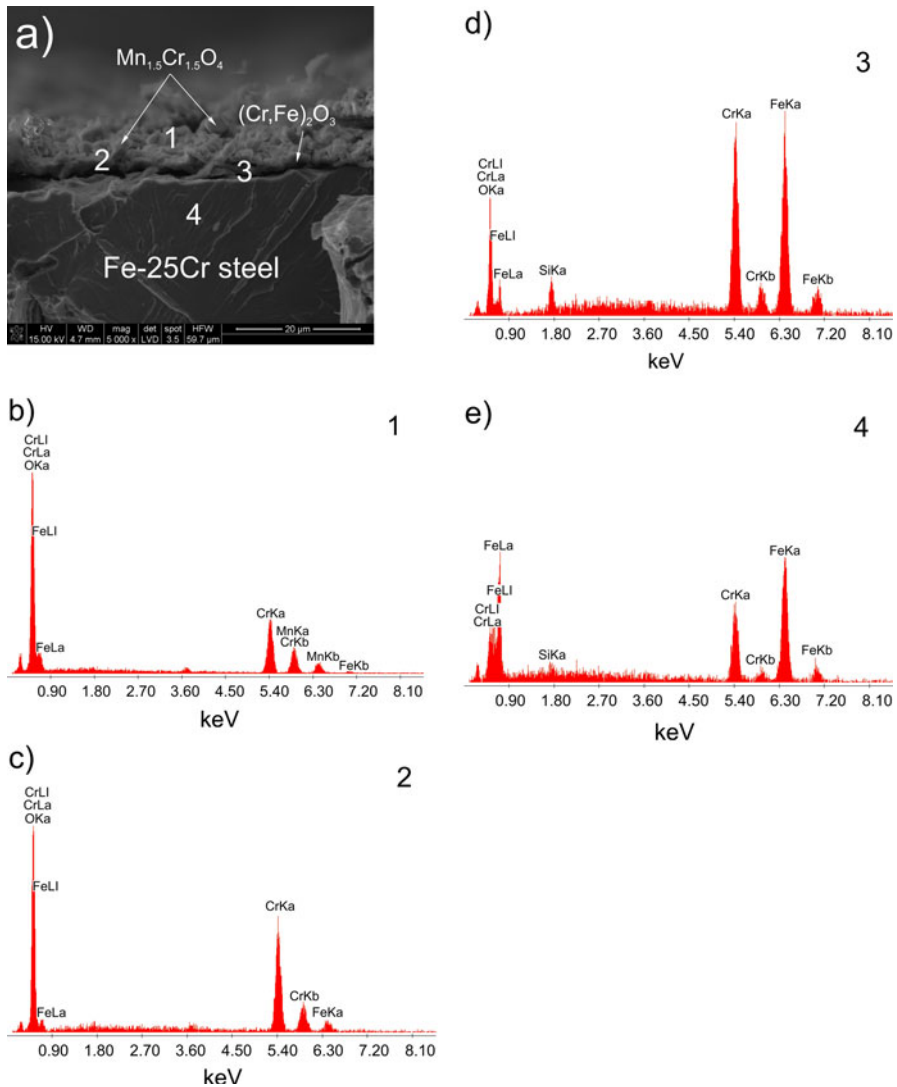
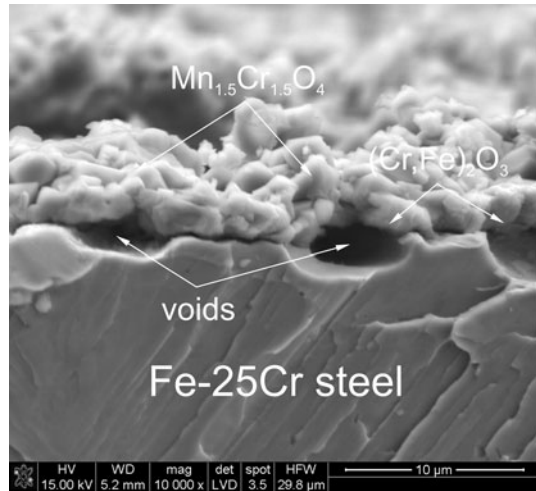


Fig. 9 a SEM fracture cross-section of the scale on Fe–25Cr after 300 h of oxidation in air at 1,073 K, b–e EDS point analysis spectra of the regions designated as 1, 2, 3 and 4

Figure 11 shows the SEM microphotograph of the fracture cross-section of the scale formed on the Fe–25Cr steel after oxidation in Ar–H₂–H₂O gas mixture at 1,073 K for 300 h and EDS point analysis (Fig. 11b). As can be seen, the duplex scale is compact and adheres well to the substrate. The average thickness of the scale is about 1.4 μm and is consistent with the kinetic data of oxidation of the Fe–25Cr steel (Fig. 2; Table 1). The oxide scale developed on pure Fe–25Cr steel in the Ar–H₂–H₂O gas mixture at 1,073 K is built of Cr₂O₃ as an inner layer, while the discontinuous, thin outer layer is composed of the Mn_{1.5}Cr_{1.5}O₄ spinel, as confirmed via X-ray diffraction

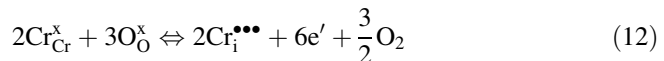
Fig. 10 SEM microphotograph of fracture cross-section of the scale on Fe–25Cr after 300 h of oxidation in air at 1,073 K



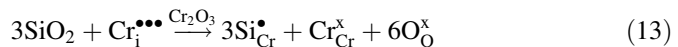
(Fig. 4b) and EDS analyses. A number of EDS analyses along the cross-section of the steel revealed a high concentration of silicon at the steel/scale interface.

Due to the fact that silicon exhibits significantly greater chemical affinity for oxygen than chromium does, internal oxidation of silicon occurs beneath the scale at the steel/ Cr_2O_3 interface, where the partial pressure of oxygen is 1.6×10^{-21} atm at 1,073 K, resulting in the formation of SiO_2 [38]. The presence of Si impurities on the level of 0.1 wt% leads to an increase in the growth rate of Cr-rich oxide scales on Cr-rich ferritic steels [39, 40]. The formation of the internal oxide precipitates of SiO_2 results in the formation of metal protrusions into the oxide scale.

Figure 12, for example, shows a TEM cross-section microphotograph illustrating isolated amorphous silica formed at the steel/scale interface. The ferritic steels that contain Si in amounts greater than 0.5 wt% usually form insulating, network-like films of silica, which may grow under the chromia scale [38]. Assuming that the predominant ionic defects at grain boundaries in Cr_2O_3 are interstitial cations, the formation of which may be represented by [14]

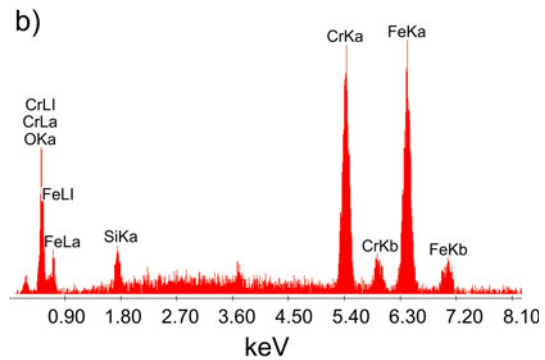
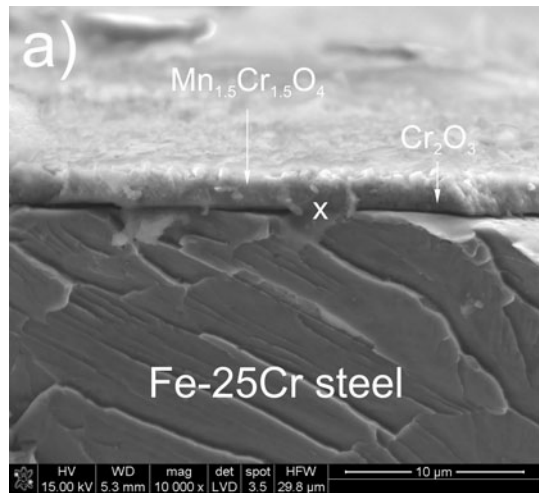


where $\text{Cr}_{\text{i}}^{\bullet\bullet\bullet}$ is the triply ionized interstitial chromium cations, e' is the quasi-free electrons and $\text{Cr}_{\text{Cr}}^{\times}$ is the chromium atom in a normal lattice site, the incorporation of the silicon into the chromia crystal lattice within the grain boundaries may be expressed by the following equation

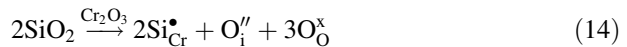


where according to the Kroger and Vink notation [40], $\text{Si}_{\text{Cr}}^{\bullet}$ is silicon at the chromium site. This equation entails that the incorporation of silicon into Cr_2O_3 grain boundaries causes a drop in the concentration of cationic defects, thereby reducing the flux of outward chromium diffusion. This tendency leads to a decrease in the corrosion rate of the studied steels. On the other hand, the incorporation of Si ions

Fig. 11 a SEM microphotograph of the cross-section of the scale on Fe–25Cr after 300 h of oxidation in Ar–H₂–H₂O at 1,073 K and **b** EDS point analysis spectra of the region designated as *x*



into the Cr₂O₃ crystal lattice might lead to increased concentrations of interstitial anions in the grain boundary area, according to the following equation



where O_i^{''} is the doubly ionized interstitial anion. Thus, silicon fulfills a “dual” function in the oxidation process. Firstly, it reduces the concentration of defects related to chromium cations within the grain boundaries of Cr₂O₃ polycrystalline. Secondly, it increases the concentration of anionic defects, which are a source of oxygen for selective oxidation of Si to SiO₂, which is deposited in the form of discontinuous inclusions within the steel/scale interface (Fig. 12).

The oxide scales formed on pure Fe–25Cr steel after oxidation in air and the Ar–H₂–H₂O gas mixture exhibited substantially different surface morphology and adhesion to the metallic core. In general, the exposure of the tested steels to the atmospheres containing hydrogen and water vapor leads to better adhesion of oxidation products (Fig. 11) compared to the corrosion reactions carried out in air (Fig. 9). In numerous studies[5, 13, 23, 41–52], a phenomenon similar to the effect of water vapor on the growth mechanism of Cr₂O₃ scale is also observed during the

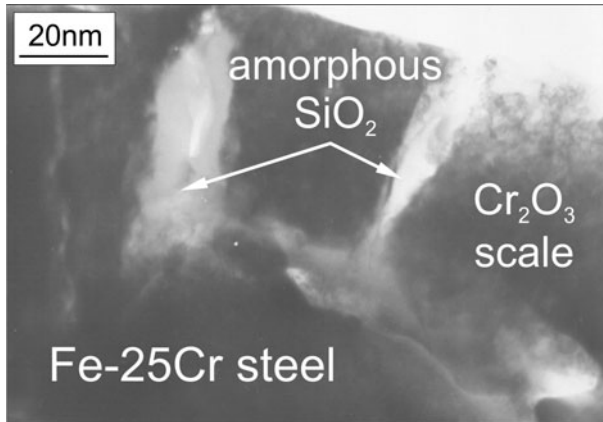


Fig. 12 TEM cross-section showing amorphous silica formed at the scale/substrate interface after 300 h of oxidation in air at 1,073 K

oxidation of pure chromium and nickel-based alloys and Ni–Cr. The chemical potential of oxygen in water vapor, and even more so in the Ar–H₂–H₂O gas mixture, is many times lower than the chemical potential of oxygen in air. Therefore, the morphology of scales formed on the same metallic substrate is different for water vapor environments and for air. In the presence of water vapor, most Cr₂O₃ grains on the scale surface are observed in the form of thin plates and whiskers, while at the steel/scale interface an inner layer with a fine-crystalline structure is often observed. Michalik et al. [48], show that the microstructure of the steel/scale interface, and also the scale adhesion to the substrate, depend not only on the partial pressure of oxygen, but also to a large degree on the partial pressure of H₂O vapor, which, when present, effectively reduces the formation of voids in the afore-mentioned interfacial region due to condensation vacancies as a result of selective oxidation of Cr.

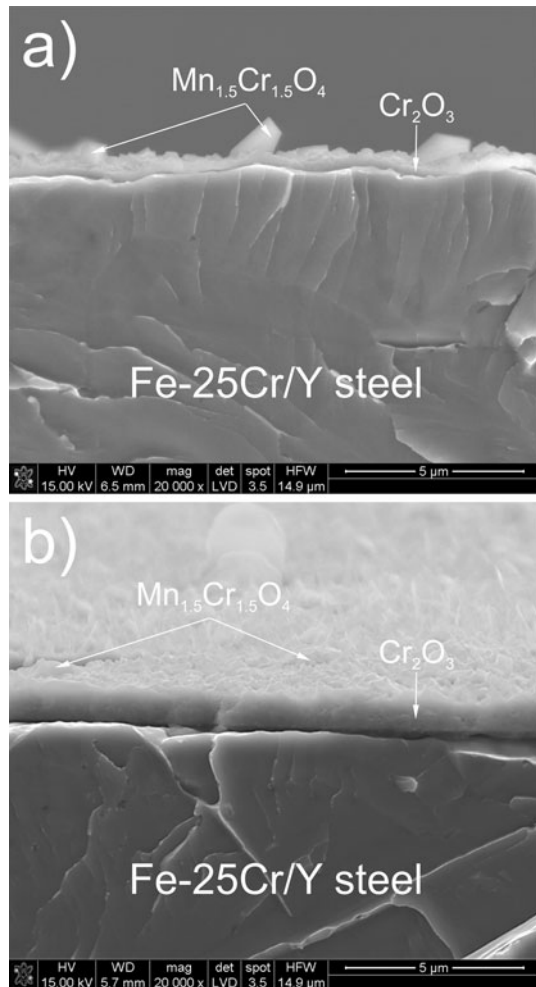
Figures 13 and 14 show the SEM microstructures of the fracture cross-sections of scales formed on the Fe–25Cr/Y and Fe–25Cr/Y₂O₃ steels after oxidation at 1,073 K for 300 h in air (Figs. 13a, 14a) and the Ar–H₂–H₂O gas mixture (Figs. 13b, 14b). The resulting scales are compact and adhere very well to the substrate, with an average thickness ranging from 0.25 to 0.55 μm, which is consistent with the kinetics data of oxidation of the studied steels.

It is worth noting that the scale formed on the Fe–25Cr/Y steel after oxidation in the Ar–H₂–H₂O gas mixture is composed of thin plates and whiskers (Fig. 13b). Such morphology should be associated with the presence of hydrogen in the afore-mentioned atmosphere, which may affect the point defect structure in the chromia. When hydrogen is incorporated into the Cr₂O₃ scale and hydride anions (H_i[–]) are formed according to the equation given below [47]



an increase in the concentration of interstitial chromium cations is observed with the decrease in the partial pressure of oxygen, according to the relation

Fig. 13 SEM microphotographs of the cross-sections of scales on Fe–25Cr/Y after 300 h of oxidation at 1,073 K in: **a** air and **b** Ar–H₂–H₂O

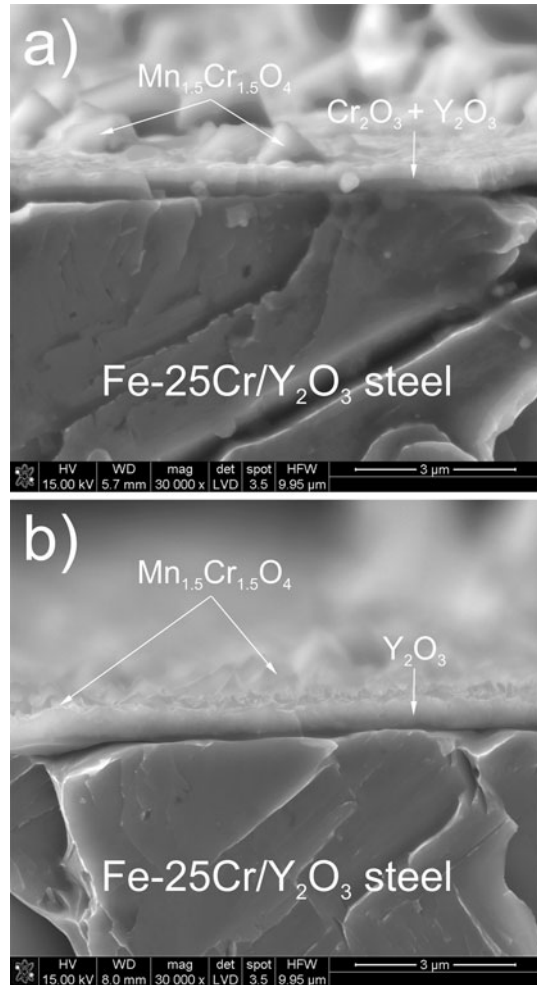


$$[Cr_i^{\bullet\bullet}] = \left(\frac{K_{12}}{27}\right)^{1/4} \frac{(1 + K_{15} \cdot p_{H_2}^{1/2})^{1/4}}{p_{O_2}^{3/16}} \quad (16)$$

where K_{12} and K_{15} is the equilibrium constants of reactions (12) and (15), respectively. From this equation it may be concluded that the conditions in the interior of the Cr₂O₃ layer may favor the formation of lamellar forms, the growth rate of which is controlled by the transport of chromium ions along grain boundary dislocations, known as surface tunnel diffusion [53].

No voids were observed at the Fe–25Cr/Y/scale and Fe–25Cr/Y₂O₃/scale interfaces during morphological observations. This indicates that the oxidation of these steels proceeds through a different mechanism than the one observed in the case of pure Fe–25Cr steel. While investigating the corrosion process of the

Fig. 14 SEM cross-sections of scales on Fe-25Cr/Y₂O₃ after 300 h of oxidation at 1,073 K in: **a** air and **b** Ar-H₂-H₂O



Co-40Cr and Fe-25Cr-1Al alloys implanted with yttrium, Przybylski and Yurek [14] showed that the difference in the corrosion process of pure material and of implanted materials grew more pronounced with oxidation time. The Cr₂O₃ scale on the non-implanted alloys grows outwardly, and its newly formed grains gradually increase their size. On the other hand, a significantly thinner Cr₂O₃ scale is formed on the implanted alloys via inward growth, and it preserves very fine grains over the whole oxidation process. The change in the dominant mass transport mechanism from the outward diffusion of chromium cations to the inward diffusion of oxygen yields a significant improvement in the adhesion of the Cr₂O₃ to the metallic core due to the absence of voids at the steel/scale interface. The reduction in the growth rate of the scales is explained by Przybylski and Yurek [14] as follows: the fine-grained scale formed on the alloys implanted with yttrium exhibits a high density of grain boundaries, which causes the inward diffusion of oxygen throughout the grain boundary to increase, and, in addition, yttrium highly segregates into grain

boundaries. Based on these studies the cited author postulated that yttrium forms perovskite YCrO_3 particles within the chromia grain boundaries. Due to the very high activation energies of the two metals in the yttrium-chromite perovskite, only oxygen vacancies are formed. According to the same author [14], YCrO_3 perovskite present at grain boundaries in the form of single molecules, or one or more monolayers of this compound, blocks the growth of the Cr_2O_3 grains and strongly inhibits the outward transport of Cr, allowing only the slowest inward diffusion of oxygen along the grain boundaries of chromia. The role of yttrium in the “grain boundaries engineering” thus refers to its ability to block the mobility of the chromia grain boundaries, preventing grains from developing into the column structure typical for the scales formed on pure Fe–25Cr steel.

Electrical Resistivity Measurements of Pure Fe–25Cr Steel/Scale and Surface-Modified Steel/Scale Systems

Connecting individual cells in a stack requires the use of interconnects, i.e. electron conductors. Thus, the interconnect material must provide a low ASR, which should not exceed $0.1 \Omega \text{ cm}^2$ [8]. Due to passivation of the surface of ferritic steel interconnects in SOFC operating conditions with chromia layers that grow according to the parabolic rate law, ASR increases. The electrical properties of pure and surface-modified Fe–25Cr steels are therefore determined mainly by the physicochemical properties of Cr_2O_3 scales and their adhesion to the metallic substrate.

Park and Natesan [54] first measured the electrical conductivity of thermally grown Cr_2O_3 scales on the surface of pure chromium using the two- and four-probe methods. These studies showed that both the electrical conductivity and the activation energy of conductivity of this scale were comparable to those exhibited by sintered chromium oxide. According to the authors [54] the activation energy of the steel/scale system may be expressed as

$$E_a = \Delta H_m + \Delta H_i + \Delta H_j \quad (17)$$

where ΔH_m is the enthalpy change of polaron movement in the Cr_2O_3 crystal lattice [eV], ΔH_i and ΔH_j is the activation energies of the electrons hopping through the electrode/scale and scale/steel interfaces, respectively [eV]. For the scales containing mainly chromium oxide, changes in terms of ΔH_m may be the effect of doping, while the remaining components of the activation energy, namely ΔH_i and ΔH_j , depend on the type of electrode used to measure the electrical conductivity and the conditions of oxidation of the metallic substrate, respectively. Liu et al. [55] have also attempted to determine the transport properties of chromia scales formed on the Ni–20Cr alloy using the blocking-electrode method. Two temperature ranges of conductivity were distinguished for chromia formed on the afore-mentioned alloy. Namely, in the range of high temperatures ($>973 \text{ K}$), intrinsic electron defects prevail and the activation energy is equal to 1.7 eV, whereas in the range of low temperatures (573–973 K) the conductivity is governed by ions and electrons, the activation energies for which are 0.3 and 0.6 eV, respectively [55].

The findings made in several studies [8, 21, 28, 55–57] suggest that the RE elements introduced into the ferritic steel as alloying elements or included in the protective coatings on the steel may significantly affect the level of electrical resistance of the entire steel/scale system. Seo et al. [28] found that the addition of some alloying elements such as Y, La and Ce in the Fe–22Cr–0.5Mn alloy oxidized in air at 1,073 K for 100–200 h favors the reduction in the ASR. According to Liu et al. [55] the presence of yttrium oxide particles in the chromia scale formed on the Ni–20Cr alloy after oxidation at 1,173 K in the H_2 – H_2O gas mixture for 24 h effectively reduces the ionic component of the total electrical conductivity of the steel/scale system. This is associated with decreased interstitial outward diffusion of Cr cations during the growth of the chromia scale. The cited authors [55] also proved the lack of influence of the Y_2O_3 particles on the conductivity of the Cr_2O_3 scale. According to Huang et al. [21] coatings containing RE elements in many cases account for a significant reduction in the electrical resistance of the steel/coating system. Larring et al. [56], who studied the effect of water vapor on the electrical conductivity of the ODS ($Cr_5Fe + Y_2O_3$) alloy covered with a Ce-containing coating, found that the electrical conductivity of such a layered composite increases with increasing water vapor pressure and decreases for increasing temperatures. Further studies by these authors [57] showed that using a coating in the LSM + LSC configuration may significantly improve the conductivity of this alloy.

The ASR of the Fe–25Cr/scale, Fe–25Cr/Y/scale and Fe–25Cr/ Y_2O_3 /scale systems, measured for temperatures of up to 1,073 K in air, are presented in Fig. 15 in an Arrhenius plot. Before the measurements, pure Fe–25Cr steel and the steel modified by implanting yttrium underneath its surface using ion implantation (Fe–25Cr/Y) or by depositing yttria on its surface (Fe–25Cr/ Y_2O_3) were isothermally

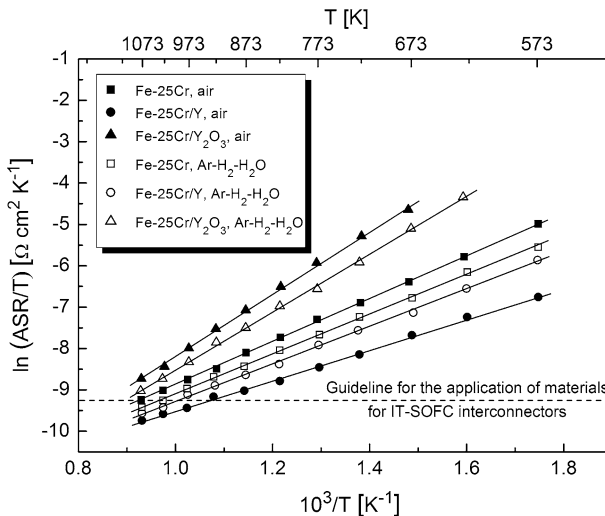


Fig. 15 Temperature dependence of ASR for Fe–25Cr/scale, Fe–25Cr/Y/scale and Fe–25Cr/ Y_2O_3 /scale systems, obtained after 300 h of pre-oxidation of steel at 1,073 K in different atmospheres

pre-oxidized in air and in the Ar–H₂–H₂O gas mixture at 1,073 K for 300 h. The plots are nearly linear over the whole temperature range (573–1,073 K), indicating thermally-activated conductivity of the samples.

According to the data [21, 54] electron carrier transport in the studied systems likely occurs via small polaron hopping in the crystal lattice of chromia, which in most cases is the main component of scales included in steel/scale systems. The ASR of the tested samples may thus be expressed in the form [8]

$$\frac{\text{ASR}}{T} = 2 \frac{\sqrt{k_{p,ef}^{\circ} \cdot t}}{\sigma^{\circ}} \exp\left(\frac{-(1/2)E_o + E_c}{kT}\right) = A \exp\left(\frac{E_a}{kT}\right) \quad (18)$$

where $k_{p,ef}^{\circ}$, σ° and A is the pre-exponential constants, expressed in [$\mu\text{m}^2 \text{s}^{-1} \text{K}^{-2}$], [$\Omega^{-1} \text{cm}^{-1}$] and [$\Omega \text{cm}^2 \text{K}^{-1}$], respectively, t is the oxidation time [s], E_o is the activation energy of oxidation [eV], E_c is the activation energy of small polaron hopping [eV], k is the Boltzmann constant [eV K^{-1}] and T is the absolute temperature [K].

Since the degree of oxidation of the investigated samples during the measurement of electrical resistance for up to 1 h at any given temperature is practically negligible, it may therefore be assumed that the activation energy of electrical conductivity (E_c) is approximately equal to E_a . The linear character of the $\log(\text{ASR}/T) = f(1/T)$ relationship makes it possible to calculate the activation energy of conductivity (E_a) of the investigated samples using the least square method, according to Eq. (18). The activation energy determination error does not exceed 0.01 eV, while the resistivities varied by less than ca. 8 % for any given temperature and for ASR values greater than 0.08 Ωcm^2 .

Table 2 presents the full set of values of specific area resistance of the Fe–25Cr/scale, Fe–25Cr/Y/scale and Fe–25Cr/Y₂O₃/scale systems at 1,073 K, and the determined activation energies of electrical conductivity (E_a) of the samples in the temperature range of 573–1,073 K, obtained after oxidation of the pure and surface-modified Fe–25Cr steels in different atmospheres. These data show that increased electrical resistance of the samples results in a subsequent increase in activation energy of conductivity. Of the studied samples, the lowest electrical resistance and also the lowest activation energy of conductivity equal to 0.32 eV was exhibited by

Table 2 Values of area specific resistance (ASR) for steel/scale systems at 1,073 K and activation energies (E_a) calculated for the investigated samples pre-oxidized at 1,073 K for 300 h in different atmospheres

Material	Pre-oxidizing atmosphere (300 h)	ASR [Ωcm^2]	E_a [eV]
Fe–25Cr	Air	0.1068	0.45
Fe–25Cr	Ar–H ₂ –H ₂ O	0.0841	0.41
Fe–25Cr/Y	Air	0.0637	0.32
Fe–25Cr/Y	Ar–H ₂ –H ₂ O	0.0765	0.39
Fe–25Cr/Y ₂ O ₃	Air	0.1721	0.65
Fe–25Cr/Y ₂ O ₃	Ar–H ₂ –H ₂ O	0.1307	0.60

the Fe–25Cr steel modified by implanting yttrium underneath its surface using ion implantation and pre-oxidized in air (Fig. 15). The ASR of the afore-mentioned sample at 1,073 K was equal to $0.0637 \Omega \text{ cm}^2$ (Table 2). Other authors have reported ASR values as low as $0.015 \Omega \text{ cm}^2$ at 1,073 K for the Fe–22Cr–0.5Mn steel containing 0.06 wt% Y and pre-oxidized in air for 100 h [28]. As will be explained later, such a low value of ASR is directly related to the low thickness of the scale related to the shorter oxidation times compared to the heat-treatment time of the studied samples (100 vs 300 h).

Although corrosion resistance of the Fe–25Cr steel modified by depositing yttria on its surface using MOCVD is the best among the tested samples (Fig. 2, Table 1), this modification yields the worst electrical properties, regardless of the type of oxidizing atmosphere (Fig. 15). This is related to the high electrical resistance of the Y_2O_3 layer [58–62] found in the scale (Figs. 5c, 7c). Numerous works dedicated to the research of point defect structure and electrical conductivity of pure and doped mono- and polycrystalline yttrium oxide have reported that regardless of the type of dopant and its concentration, Y_2O_3 is p-type semiconductor at high temperatures and for high oxygen partial pressures. [60–62] The conductivity of this oxide is predominantly determined by the ionic component. [60–62] Due to the large discrepancies in the values of conductivity and activation energy it is difficult to clearly determine which of the Y_2O_3 sublattices controls the ionic conductivity of this compound. [60–62]

The ASR of the Fe–25Cr/scale system obtained after the oxidation of pure steel in air and the ASR of the Fe–25Cr/ Y_2O_3 steel pre-oxidized in both atmospheres exceed the acceptable ASR level of $0.1 \Omega \text{ cm}^2$ over the entire investigated temperature range. The reason for the deterioration in the electrical properties of the Fe–25Cr/scale system is poor adhesion of the scale to the metal substrate (Figs. 9a, 10). Differences in the activation energies of conductivity of the studied Fe–25Cr/scale and Fe–25Cr/Y/scale systems pre-oxidized in both reaction atmospheres may be attributed to ΔH_m and ΔH_j (Eq. (12)), assuming that ΔH_i is constant due to the application of only a single type of electrode (Pt electrode) for electrical resistance measurements. It should be noted that the evaluated activation energies (E_a) are comparable to the values reported by other researchers [63]. Due to the fact that the adhesion of the scale formed on the pure Fe–25Cr steel after oxidation in the Ar– H_2 – H_2O gas mixture is much better than after oxidation in air, the ASR level of the Fe–25Cr/scale system after oxidation in the former atmosphere is significantly lower compared to the ASR of this system after oxidation in air. The fact that the ASR of the Fe–25Cr/Y/scale system obtained after the oxidation of the Y-modified steel in Ar– H_2 – H_2O is higher than after heat-treatment in air might be explained by the formation of amorphous SiO_2 precipitates at the steel/scale interface.

Summary

Kinetic studies carried out under isothermal conditions at 1,073 K in air and the Ar– H_2 – H_2O gas mixture showed that the corrosion resistance of Fe–25Cr significantly improved after surface modification via Y implantation at the surface or via deposition of a Y_2O_3 layer on the surface using MOCVD. The growth of scales on

the unmodified and modified steels approximately followed the parabolic rate law. The oxidation constants for the above-mentioned samples in both atmospheres were in the range from 10^{-15} to around 10^{-14} $\text{g}^2 \text{cm}^{-4} \text{s}^{-1}$, and were typical of the group of alloys known as “chromia formers”. It was found that oxidation in the above-mentioned conditions results in the formation a protective Cr_2O_3 layer on the surface of the pure and surface-modified Fe–25Cr steels. This layer exhibited very satisfactory adhesion to the metallic core for all samples except pure steel oxidized in air. Furthermore, the $\text{Mn}_{1.5}\text{Cr}_{1.5}\text{O}_4$ spinel in the form of thin outer layers or separate precipitates was identified. The presence of this spinel on the surface of the scale suppresses the formation of volatile chromium compounds. Measurements of the rate of chromium vaporization from the surface of the scales formed on the studied steel samples in flowing air– H_2O mixture at 1,073 K revealed that the scale formed on the surface-modified steel may successfully play the role of a barrier against the formation of volatile chromium compounds. Resistance measurements conducted for the investigated steel/scale systems showed that the steel after yttrium implantation exhibits the lowest ASR, which remains in the range required for SOFC application for all temperatures between 973 and 1,073 K. On the other hand, the ASR values observed for pure steel and the steel with the deposited Y_2O_3 layer exceeded the acceptable limit. It may thus be concluded that only the yttrium-modified steel is a material with the potential to be used in the fabrication of interconnects designed for application in planar-type IT-SOFCs.

Acknowledgments This work was done as part of the statutory activities of the Department of Physical Chemistry and Modeling, Faculty of Materials Science and Ceramics, AGH University of Science and Technology (Contract No. 11.11.160.257-4). The authors are grateful to Dr. Boguslaw Rajchel from The Henryk Niewodniczański Institute of Nuclear Physics Polish Academy of Science, Krakow, for his assistance in the implantation of yttrium in the ferritic steel.

Open Access This article is distributed under the terms of the Creative Commons Attribution License which permits any use, distribution, and reproduction in any medium, provided the original author(s) and the source are credited.

References

1. N. Q. Minh, T. Takahashi, *Science and Technology of Ceramic Fuel Cells* (Elsevier, Amsterdam, 1995).
2. S. C. Singhal and K. Kendall (eds.), *High Temperature Solid Oxide Fuel Cells: Fundamentals, Design and Applications* (Elsevier, Kidlington Oxford, 2003).
3. J. W. Fergus, *Journal of Power Sources* **147**, 46 (2005).
4. Z. Yang, K. S. Weil, D. M. Paxton, and J. W. Stevenson, *Journal of the Electrochemical Society* **150**, A1188 (2003).
5. W. J. Quadackers, J. Piron-Abellan, V. Shemet, and L. Singheiser, *Materials at High Temperatures* **20**, 115 (2003).
6. J. W. Fergus, *Materials Science and Engineering A* **397**, 271 (2005).
7. T. Brylewski, M. Nanko, T. Maruyama, and K. Przybylski, *Solid State Ionics* **143**, 131 (2001).
8. W. Z. Zhu and S. C. Deevi, *Materials Research Bulletin* **38**, 957 (2003).
9. K. Przybylski, T. Brylewski, and J. Morgiel, *Materials Science Forum* **461–464**, 1099 (2004).

10. T. Brylewski, J. Dąbek, K. Przybylski, J. Morgiel, and M. Rękas, *Journal of Power Source* **208**, 86 (2012).
11. K. Hilpert, D. Das, M. Miller, D. H. Peck, and R. Weiß, *Journal of the Electrochemical Society* **143**, 3642 (1996).
12. T. Kadowaki, T. Shiomitsu, E. Matsuda, H. Nakagawa, H. Tsuneizumi, and T. Maruyama, *Solid State Ionics* **67**, 65 (1993).
13. P. Kofstad, *High Temperature Corrosion*, (Elsevier Applied Science, Essex, England, 1988).
14. K. Przybylski and G. J. Yurek, *Materials Science Forum* **43**, 1 (1989).
15. G. Bonnet, M. Silva, S. Chevalier, J. P. Larpin, and J. C. Colson, *Surface and Coating Technology* **80**, 76 (1996).
16. J. Piron-Abellan and W. J. Quadackers, Report Forschungszentrum Jülich FRG, Jül-4170, ISSN 0944-2952 (2005).
17. B. Rajchel, M. Drwiega, E. Lipińska, and M. Wierba, *Nuclear Instruments and Methods in Physical Research Section B* **89**, 342 (1994).
18. S. Chevalier, G. Bonnet, and J. P. Larpin, *Applied Surface Science* **167**, 125 (2000).
19. K. Przybylski, J. Prazuch, T. Brylewski, and T. Maruyama, in *Proceedings 14th International Corrosion Congress, CorrISA, Cape Town, South Africa* 2, 1 (1999).
20. T. Brylewski and K. Przybylski, *Annales de Chimie Science des Matériaux* **33**, 75 (2008).
21. K. Huang, P. Y. Hou, and J. B. Goodenough, *Solid State Ionics* **129**, 237 (2000).
22. N. Birks, G. H. Meier, and E. S. Pettit, *Introduction to the High-temperature Oxidation of Metals*, (Published by Cambridge University Press, Cambridge, UK, 2006).
23. S. Mrowec and T. Werber, *Modern Scaling-Resistant Materials*, (National Bureau of Standards and National Science Foundation, Washington DC, 1982).
24. X. Chen, P. Y. Hou, C. P. Jacobson, S. J. Visco, and L. C. D. Jonghe, *Solid State Ionics* **176**, 425 (2005).
25. N. Babu, R. Balasubramaniam, and A. Ghosh, *Corrosion Science* **43**, 2239 (2001).
26. J. Stringer, B. A. Wilcox, and R. I. Jaffe, *Oxidation of Metals* **5**, 11 (1972).
27. M. H. La Branche and G. J. Yurek, Annual Progress Report, DOE Contract No. DE-AC-02-79ER-10507, Department of Energy, Gaithersburg, MD (1984).
28. H. S. Seo, G. Jin, J. H. Jun, D.-H. Kim, and K. Y. Kim, *Journal of Power Sources* **178**, 1 (2008).
29. W. Qu, L. Jian, D. G. Ivey, and J. M. Hill, *Journal of Power Sources* **157**, 335 (2006).
30. E. Konycheva, H. Penkalla, E. Wessel, U. Seeling, L. Singheiser, and K. Hilpert, in *Solid Oxide Fuel Cells IX (SOFC IX): Electrochemistry Society Proceedings PV 2005-07*, eds. S. C. Singhal and J. Mizusaki, (The Electrochemical Society, Pennington, 2005) p. 1874.
31. E. Konycheva, H. Penkala, E. Wessel, J. Mertens, U. Seeling, L. Singheiser, and K. Hilpert, *Journal of the Electrochemical Society* **153**, A765 (2006).
32. JADE Version 7 Software—XRD Processing Identification and Quantification, Materials Data, Inc., 2004.
33. M. G. E. Cox, B. McEnaney, and V. D. Scott, *Philosophical Magazine B* **26**, 839 (1972).
34. F. Riffard, H. Buscail, E. Caudron, R. Cuffe, C. Issartel, and S. Perrier, *Applied Surface Science* **199**, 107 (2002).
35. M. J. Cristobal, P. N. Gibson, and M. F. Stroosnijder, *Corrosion Science* **38**, 805 (1996).
36. E. Tondo, M. Boniardi, D. Cannoletta, M. F. De Riccardis, and B. Bozzini, *Journal of Power Sources* **195**, 4772 (2010).
37. S. Mrowec, *Corrosion Science* **7**, 563 (1967).
38. R. A. Rapp, *Corrosion* **21**, 382 (1965).
39. P. Huczowski, N. Christiansen, V. Shemet, L. Niewolak, J. Piron-Abellan, L. Singheiser, and W. J. Quadackers, *Fuel Cells* **06**, 93 (2006).
40. F. Kröger, *The Chemistry of Imperfect Crystals*, (North Holland, Amsterdam, 1964).
41. G. J. Yurek, Annual Progress Report, DOE Contract No. DE-AC-02-79ER-10507, Department of Energy, Gaithersburg, MD (1985).
42. J. G. Crouch and J. C. Scully, *Oxidation of Metals* **15**, 101 (1981).
43. Y. Ikeda and K. Nii, *Transactions of the Japan Institute of Metals* **26**, 52 (1984).
44. W. J. Quadackers, J. F. Norton, S. Canetoli, K. Schuster, and A. Gil, in *Proceedings 3rd Conference on Microscopy of Oxidation*, eds. S. B. Newcomb and J. A. Little, (The Institute of Metals, London, 1996) p. 185.
45. A. Galerie, Y. Wouters, and M. Caillet, *Materials Science Forum* **369–372**, 231 (2001).

46. S. Henry, J. Mougin, Y. Wouters, J. P. Petit, and A. Galerie, *Materials at High Temperatures* **17**, 231 (2000).
47. M. Hänsel, W. J. Quadakkers, and D. J. Young, *Oxidation of Metals* **59**, 285 (2003).
48. M. Michalik, M. Hänsel, J. Žurek, L. Singheiser, and W. J. Quadakkers, *Materials at High Temperatures* **22**, 213 (2005).
49. J. Žurek, E. Wessel, L. Niewolak, F. Schmitz, T.-U. Kern, L. Singheiser, and W. J. Quadakkers, *Corrosion Science* **46**, 2301 (2004).
50. E. Essuman, G. H. Merier, J. Žurek, M. Hänsel, L. Singheiser, and W. J. Quadakkers, *Scripta Materialia* **57**, 845 (2007).
51. E. Essuman, G. H. Merier, J. Žurek, M. Hänsel, T. Norby, L. Singheiser, and W. J. Quadakkers, *Corrosion Science* **50**, 1753 (2008).
52. J. Žurek, D. J. Young, E. Essuman, M. Hänsel, H. J. Penkala, L. Niewolak, and W. J. Quadakkers, *Materials Science and Engineering A* **477**, 259 (2008).
53. L. Mikkelsen and S. Linderöth, *Materials Science and Engineering A* **361**, 198 (2003).
54. J. H. Park and K. Natesan, *Oxidation of Metals* **33**, 31 (1990).
55. H. Liu, M. M. Stack, and S. B. Lyon, *Solid State Ionics* **109**, 247 (1998).
56. Y. Larring, R. Haugrud, and T. Norby, *Journal of the Electrochemical Society* **150**, B374 (2003).
57. Y. Larring and T. Norby, *Journal of the Electrochemical Society* **147**, 3251 (2000).
58. T. Norby and P. Kofstad, *Journal of the American Ceramic Society* **67**, 786 (1984).
59. T. Norby and P. Kofstad, *Solid State Ionics* **20**, 169 (1986).
60. N. M. Tallan and R. W. Vest, *Journal of the American Ceramic Society* **49**, 401 (1966).
61. J. Schieltz, J. W. Patterson, and D. R. Wilder, *Journal of the Electrochemical Society* **118**, 1140 (1971).
62. G. V. SubbaRao, S. Ramdas, P. N. Mehrotra, and C. N. R. Rao, *Journal of Solid State Chemistry* **2**, 377 (1970).
63. I. Antepará, I. Villarreal, L. M. Rodríguez-Martínez, N. Lecanda, U. Castro, and K. Laresgoiti, *Journal of Power Source* **151**, 103 (2005).